More accurate macro-models of solid oxide fuel cells through electrochemical and microstructural parameter estimation - Part II: Parameter estimation

Published in Journal of Power Sorces Volume 286, 15 July 2015, Pages 321–329

More accurate macro-models of solid oxide fuel cells through electrochemical and microstructural parameter estimation – Part II: Parameter estimation

Carlos Boigues-Muñoz[1,2,*], Davide Pumiglia[2,3], Stephen J. McPhail[2], Giulio Santori[4], Dario Montinaro[5] Gabriele Comodi[1], Maurizio Carlini[3], Fabio Polonara[1]

[1] Dipartimento di Ingegneria Industriale e Scienze Matematiche, Università Politecnica delle Marche, Via Brecce Bianche, Polo Montedago, 60131 Ancona, Italy
[2] UTRINN, ENEA C.R. Casaccia, Via Anguillarese 301, 00123 Rome, Italy
[3] DAFNE, Università degli Studi della Tuscia, Via S. Camilo de Lellis snc, 01100 Viterbo, Italy
[4] The University of Edinburgh, School of Engineering, Institute for Materials and Processes, Mayfield Road, The King's Buildings, EH9 3JL, Edinburgh, UK
[5] SOFCpower SpA, Viale Trento 115/117, 38017Mezzolombardo (Trento), Italy

Abstract

This paper presents a systematic synergetic approach between experimental measurements, equivalent circuit modelling (described in Part I) and macro-scale modelling theory which has proved to be instrumental for the estimation of microstructural and electrochemical features of a Ni-YSZ|YSZ|$Pr_2NiO_{4+\delta}$ – GDC solid oxide fuel cell (SOFC). The aforementioned parameters have been used to generate a more accurate CFD macro-model which has been validated against the experimental results (presented in Part III).

Keywords: Butler-Volmer; Overpotentials; SOFC; Tortuosity.

1. Introduction

After decades of research and development, the first generation of SOFC technology-based combined heat and power (CHP) devices are finally leaving the production line towards demonstration plants and early-market consumers. Alas, these systems cannot yet fully compete with traditional power generation technologies in terms of robustness, reliability and cost-effectiveness, thus a profound and systematic research of basic materials and elements is still needed in order to improve the lifetime span, targeting a second generation which should be able to withstand more than forty thousand hours of continuous operation with a low performance degradation rate (<0.1%/kh) [1,2].

Since the mid 1990's with the advent of the first fuel cell models (as an example and naming the most influential ones: Achenbach *et al.* [3], Virkar *et al*. [4] and Yakabe *et al.* [5]) until nowadays, little has changed in the interaction between experimental and modelling fields, being often too disjoined and not operating in full awareness of each other. A vast number of articles found in literature deal with modelling the immediate performance of SOFCs when varying one or more operating parameters such as temperature, gas composition and cell potential [6], nevertheless, most of these works employ microstructural and electrochemical modelling parameters (i.e.

porosity, tortuosity, exchange current density, *etc…*) from other works rather than from experimental data obtained for the specific type of cell being modelled, detracting to some extent from the soundness of the model and hence from the validity of the results. It is crucial to generate a model which encompasses realistic data from the SOFC being studied in order to not only get a robust model which can predict reasonably well the immediate performance of the cell, but most importantly to go one step beyond the state-of-the-art and start predicting the effects of degradation phenomena in the concerned type of cell. Attending to the abovementioned requests, it seems undisputable how the use of novel analysis tools and techniques is the fundamental pillar on which the future models must rest.

The work reported in this article is a compendium of how to employ the experimental results obtained from a specifically designed experimental campaign (fully described in Part I) to estimate the microstructural and electrochemical parameters driving the operation of the SOFC button cell in order to employ them in a CFD macro-model (fully described in Part III).

2. Parameter estimation

2.1 Experimental results

Estimation of the modeling parameters is done via a symbiotic approach encompassing experimental results with theoretical and semi-empirical mathematical equations. The experimental results have been presented in the second part of this work alongside the description of the thorough experimental campaign which foresaw the operation of the SOFC single cell under a number of different conditions by varying one at a time: temperature, hydrogen partial pressure in the anode, steam partial pressure in the anode and oxygen partial pressure in the cathode. For each of the conditions an electrochemical impedance spectroscopy (EIS) measurement was carried out and then fitted by means of the equivalent circuit model (ECM) depicted in Fig. 1 (see Part I for an extensive explanation on how this ECM was obtained). Each of the electrical elements of the ECM represent a precise physicochemical process occurring in the SOFC, thus it is possible to quantitatively associate a resistance value to a particular process and monitor how this modifies according to the operating conditions.

➔ **Figure 1**

2.2 Assumptions and considerations

The test station configuration, the relatively small active area of the button cell and the high volumetric flow rates of the gases used enable to take into consideration a number of assumptions that render simpler the procedure of obtaining the modelling parameters with small information loss or deviance. These assumptions and considerations are hereby listed:

- *One-dimensional domain*: on the one hand gas concentrations along the fuel and air channels are uniform because of the high molar flows being employed, thus, even when not operating under OCV conditions the fuel and air utilizations are rather low. On the other hand, the current density is uniform over the entire electrode attending to the aforementioned gas distributions.

- *Stationary conditions*: the testing procedures foresaw sufficient stabilization time when gas flows, temperature or current density were modified.
- *Isobaric conditions*: the pressure drop in the porous electrodes is negligible. The pressure in the system is considered to be the atmospheric one (P=101325Pa).
- *Isothermal conditions*: it has been experimentally demonstrated how the temperature of the button cell remains in a range of ±2ºC during the polarization curve even when operating at very high current densities.
- *Reactions occur only in the electrode/electrolyte interface*: even if this does not adjust to reality for cermet-type anodes and composite cathodes, this assumption is widely extended in the modelling field as the anode's and cathode's active layers are very thin when compared with the gas diffusion layer, thus they are often considered as interfaces rather than as volumes [6,7].
- *Species transport is driven only by diffusion*: velocity of the fluid inside the electrode can be neglected.
- *Negligible performance degradation*: cell performance is always evaluated before and after the electrochemical tests in order to quantify the degradation induced by these. A high degradation value would invalidate the whole procedure violating the principle of univocal state of the test specimen.

2.3 Microstructural parameter identification

2.3.1 Porosity and particle radii

The description of the methodologies employed in order to measure or estimate the anode porosity, and the particle radii in anode and cathode is present in the second part of this work (*More accurate macro-models of SOFCs through electrochemical and microstructural parameter estimation – Part I: Experimentation*). However, the values of three microstructural parameters have been hypothesized due to the difficulties in obtaining them experimentally, these are: cathode porosity, and the volume fraction of the electronic and ionic phases in both electrodes. For the first parameter (ε_{cat}) a value of 35% has been employed whilst for the last two a volume fraction of 50% was established.

2.3.2 Tortuosity

It is very difficult to determine the actual paths that molecules travel because the paths in porous materials are very complicated [8]. In this work the tortuosity has been estimated indirectly by means of the concentration overpotential resistances, which are governed by the species concentration in the TPB.

The steady-state species transport partial differential equation (PDE) is expressed by means of Eq. (1) when transport by convection is neglected and it is assumed that the electrochemical reaction occurs in the electrode/electrolyte interface.

$$\nabla \vec{J}_k = 0 \qquad (1)$$

where $\vec{J}_k$ is the diffusive flux.

The modified Stefan-Maxwell model (MSMM) has been employed to describe the multicomponent species transport in anode and cathode, namely:

$$\sum_{\substack{k=1 \\ k\neq l}}^{n} \frac{p_l \vec{J}_k - p_k \vec{J}_l}{P D_{k,l}^{eff}} + \frac{\vec{J}_k}{D_{Kn,k}^{eff}} = -\frac{1}{RT} \nabla p_k \tag{2}$$

where $D_{k,l}^{eff}$ is the effective binary diffusion coefficient between species *k* and l and $D_{Kn,k}^{eff}$ is the effective Knudsen diffusion coefficient of species *k.* The mathematical expressions of the diffusion coefficients have been extensively described in Part III of this work (*Modelling and sensitivity analysis*).

Attending to the fact that heterogeneous chemical reactions are the prevailing ones in state-of-the art SOFC electrodes [9], Graham's law of diffusion for multicomponent gases [10] must be employed to establish flux consistency in the control volume, where the former, explicitly described by means of Eq.(3) is used along with Eq.(2) to calculate the molar fluxes of the different components.

$$\sum_{k} J_k \sqrt{MW_k} = 0 \tag{3}$$

In the fuel side of the SOFC the ternary composition H_2-H_2O-N_2 was used to characterize the Ni-YSZ porous matrix. It can be demonstrated how from Eq.(1), Eq.(2) and Eq.(3) – explained thoroughly by Suwanwarangkul *et al.* in [9] – the following second-order ordinary differential equation (ODE) arises:

$$\frac{d^2 x_k}{dz^2} + \frac{\beta}{D_{H2,H2O}^{eff}} \left[\frac{1}{D_{k,N2}^{eff}} + \frac{1}{D_{Kn,k}^{eff}} + (1 - x_{N2}) \left(\frac{1}{D_{H2,H2O}^{eff}} - \frac{1}{D_{k,N2}^{eff}} \right) - \frac{\beta x_k}{D_{H2,H2O}^{eff}} \right]^{-1} \left(\frac{dx_k}{dz} \right)^2 = 0 \tag{4}$$

where *k* can be either H_2 or H_2O and the coefficient β, which accounts for the deviation from equimolar flux, is calculated as follows:

$$\beta = 1 - \sqrt{\frac{MW_k}{MW_l}} \tag{5}$$

where if *k* denotes H_2 in Eq. (4) then l denotes H_2O and *vice versa*.

The Dirichlet boundary condition is given by Eq. (6), satisfying in this way the species concentration continuity in the fuel channel and anode interface (z=0). The Neumann boundary conditions, expressed by Eq. (7) and Eq. (8) are strictly linked to hydrogen consumption and steam formation in the electrode/electrolyte interface.

$$x_k|_{z=0} = x_{k,bulk} \tag{6}$$

$$\left.\frac{dx_{H2}}{dz}\right|_{z=0} = -\frac{iRT}{2FP}\left[\frac{1}{D_{H2,N2}^{eff}} + \frac{1}{D_{Kn,H2}^{eff}} + \left(1 - x_{N2,bulk}\right)\left(\frac{1}{D_{H2,H2O}^{eff}} - \frac{1}{D_{H2,N2}^{eff}}\right) - \frac{\beta x_{H2}}{D_{H2,H2O}^{eff}}\right] \quad (7)$$

$$\left.\frac{dx_{H2O}}{dz}\right|_{z=0} = \frac{iRT}{2FP}\left[\frac{1}{D_{H2O,N2}^{eff}} + \frac{1}{D_{Kn,H2O}^{eff}} + \left(1 - x_{N2,bulk}\right)\left(\frac{1}{D_{H2,H2O}^{eff}} - \frac{1}{D_{H2O,N2}^{eff}}\right) - \frac{\beta x_{H2O}}{D_{H2,H2O}^{eff}}\right] \quad (8)$$

The molar fraction of the inert gas is immediately obtained from the molar balance equation, namely:

$$x_{H2} + x_{H2O} + x_{N2} = 1 \quad (9)$$

Even with today's computational technology, it is a troublesome issue to obtain an analytical expression of this ODE in particular, therefore a numerical solution was obtained by applying the iterative Runge-Kutta algorithm (*ode45*) present in MATLAB ®.

The following graph (Fig. 2) illustrates the concentration overpotential in the anode as a function of the current density (only calculated for very small values of i) for typical tortuosity values; the points from Fig.2 have been obtained by inserting the result from Eq. (4) into the theoretical expression of the anodic concentration overpotential, namely:

$$\eta_{conc,an} = \frac{RT}{2F} ln\left(\frac{x_{H2,bulk} \cdot x_{H2O,a/e}}{x_{H2,a/e} \cdot x_{H2O,bulk}}\right) \quad (10)$$

➔ **Figure 2**

From the aforementioned figure it can be observed how the concentration overpotential can be approximated to a first-order polynomial in the vicinities of the OCV, namely:

$$\eta_{conc,an} \approx a_0 + a_1 i \quad (11)$$

When the cell is operating under OCV conditions (i=0) the concentration overpotential is null, thus a_0 must be zero. The gradient can be obtained by differentiating Eq. (11) with respect to the current density, which is concurrently the expression for the species concentration resistance, specifically:

$$r_{conc,an} = \frac{d\eta_{conc,an}}{di} = a_1 \quad (12)$$

Recalling what has just been mentioned, it is straightforward to see that the numerical results arising from the theoretical expression of the concentration overpotential – Eq. (10) – and from

the linearized anodic concentration overpotential – Eq. (11) – can be considered to be identical in the proximities of the OCV. Since the anode tortuosity is implicitly correlated with the partial pressures (or molar fractions) by means of the effective diffusion coefficients present in the ODE expressed by Eq. (4), it is impossible to obtain an explicit function of it. However, the anode tortuosity can be estimated iteratively by guessing an initial τ_{an} and solving the following minimization problem (Eq. (13)) taking into consideration that the molar fractions are correlated with the tortuosity by means of the ODE displayed in Eq. (4). Equation (13) has to be solved setting an arbitrary small value of current density (i), so that the linearity of the concentration overpotential is not violated (see Fig. 2).

$$\min_{\tau}\left\{\left|r_{conc,an}i-\frac{RT}{2F}ln\left(\frac{x_{H2,bulk}\cdot x_{H2O,a/e}}{x_{H2,a/e}\cdot x_{H2O,bulk}}\right)\right|\right\} \tag{13}$$

where the subscript *a/e* denotes the anode/electrolyte interface. The species concentration resistance ($r_{conc,an}$) has been calculated by fitting the experimental data to the ECM.

➔ **Figure 3**

A tortuosity value of τ_{an}=3.8 has been found in the anode porous matrix when applying the previously mentioned minimization problem correlating experimental data (Fig. 3) with theoretical analysis. Tortuosity values ranging from 1.8 to 6 have been found in literature for state-of-the-art Ni-YSZ based electrodes for SOFCs [11,12], indicating how slightly different manufacturing processes can affect this morphological parameter even if the raw materials employed are identical (or really similar). The fact that this parameter cannot be measured directly and must be estimated by indirect means also aggregates a substantial uncertainty which could partly explain the wide range of values found in literature.

In the cathode side of the fuel cell the binary composition O_2-N_2 was used to characterize the $Pr_2NiO_{4+\delta}$ porous structure. Only the oxygen participates in the electrochemical reaction in the active sites, thus its molar fraction along the electrode is governed by the so-called self-diffusion mechanism [13], where its ordinary differential equation takes the following form:

$$-\frac{P}{RT}\frac{dx_{O2}}{dz}=J_{O2}\left(\frac{1}{D_{O2,N2}^{eff}}+\frac{1}{D_{Kn,O2}^{eff}}-\frac{x_{O2}}{D_{O2,N2}^{eff}}\right) \tag{14}$$

Solving the previous ODE taking into consideration that at z=0 the oxygen molar fraction is the bulk one ($x_{O2,bulk}$) and that the diffusive flux is $J_{O2}=i/(4F)$, the molar fraction along the cathode is determined by:

$$x_{O2,z}=D_{O2,N2}^{eff}\left[D_{O2}^{*}+\left(\frac{x_{O2,bulk}}{D_{O2,N2}^{eff}}-D_{O2}^{*}\right)exp\left(\frac{iRTz}{4FPD_{O2,N2}^{eff}}\right)\right] \tag{15}$$

having the diffusion coefficient D_{O2}^{*} the following expression:

$$D_{O2}^{*}=\left(\frac{1}{D_{O2,N2}^{eff}}+\frac{1}{D_{Kn,O2}^{eff}}\right) \tag{16}$$

The nitrogen molar fraction is calculated immediately from the molar conservation principle.

$$x_{N2(cat),z} = 1 - x_{O2,z} \tag{17}$$

The resistance to species concentration in the cathode/electrolyte interface for the special case of open circuit voltage is obtained by substituting Eq. (15) into the theoretical expression of the cathodic concentration overpotential (Eq. (18)) and differentiating with respect to the current density whilst setting $i = 0$ (Eq. (19)).

$$\eta_{conc,cat} = \frac{RT}{4F} ln\left(\frac{x_{O2,bulk}}{x_{O2,TPB}}\right) \tag{18}$$

$$r_{conc,cat}\big|_{i=0} = \frac{d\eta_{conc,cat}}{di}\bigg|_{i=0} = \left(\frac{RT}{4F}\right)^2 \frac{L_{cat}}{P}\left(\frac{D^*_{O2}}{x_{O2,bulk}} - \frac{1}{D^{eff}_{O2,N2}}\right) \tag{19}$$

Due to the small values of the cathode species concentration resistance, the complex nonlinear least squares (CNLS) fitting could not discern the Warburg element from the ECM for the test cases of pO_2 = 0.5 and 0.21 atm, whilst for the case of pO_2 = 0.08 atm the fitting error was significantly high. Only when the oxygen partial pressure was reduced considerably (i.e. pO_2 = 0.04 atm) the fitting software was able to clearly identify the finite length Warburg element with a relatively low error. This issue was also observed by Leonide *et al*. in [14]. For an operating temperature of 700ºC and a pO_2 of 0.04 atmospheres, the concentration resistance in the cathode was: 5.59± 0. 67 mΩ·cm^2. Substituting this value in Eq. (19) and solving for the cathode tortuosity, a value of 5.7 was obtained for this morphological parameter (τ_{cat}).

2.4 Electrochemical parameter identification

The Butler-Volmer equation, being comprised of exponential terms, can be rewritten as an infinite sum of terms (known as Taylor series) as follows:

$$i = i_0\left[\frac{n_e F\eta_{act}}{RT} + \frac{(2\alpha - 1)}{2}\left(\frac{n_e F\eta_{act}}{RT}\right)^2 + \frac{(3\alpha - 3\alpha^2 - 1)}{6}\left(\frac{n_e F\eta_{act}}{RT}\right)^3 + \cdots\right] \tag{20}$$

The exchange current density is usually expressed as an Arrhenius-type equation dependent on the temperature and on the molar fractions of the reactants and products of the semi-reactions. The expressions for the anode and cathode are respectively:

$$i_{0,an} = i^{pre}_{0,an}(x_{H2})^{\gamma_{H2}}(x_{H2O})^{\gamma_{H2O}} exp\left(-\frac{E_{act,an}}{RT}\right) \tag{21}$$

$$i_{0,cat} = i^{pre}_{0,cat}(x_{O2})^{\gamma_{O2}} exp\left(-\frac{E_{act,cat}}{RT}\right) \tag{22}$$

where $i_{0,an}^{pre}$ and $i_{0,cat}^{pre}$ are the exchange transfer current density pre-exponential factor in the anode and cathode respectively, $E_{act,an}$ and $E_{act,cat}$ the activation energies for anode and cathode and γ_k is the reaction order of species *k*.

For very small overpotentials a first-order approximation of Eq. (20) can be made with a negligible error, producing a linear relationship between the activation overpotential and the current density (Eq. (23)). As the EIS measurements have been carried out under OCV conditions with a small excitation signal (ΔE=10mV), the abovementioned condition is valid.

$$i \approx i_0 \frac{n_e F \eta_{act}}{RT} \tag{23}$$

Equation (24) stems from Eq. (23) and expresses the activation overpotential as a function of the current density, being valid only for very small values of i.

$$\eta_{act} \approx \frac{RT}{n_e F} \frac{i}{i_0} \tag{24}$$

The resistance associated to the activation overpotential is calculated by differentiating the activation overpotential with respect to the current density, namely:

$$r_{act} \approx \frac{RT}{n_e F i_0} \tag{25}$$

2.4.1 Anode exchange current density

Substituting the anode local exchange transfer current density in Eq. (25) by its Arrhenius-type expression defined by Eq. (21) and taking into consideration that two electrons take part in the electrochemical reaction per mole of H_2 reacted (ergo, n_e=2), the resistance related to the anodic activation overpotential (associated to charge transfer mechanisms) is expressed in the following terms:

$$\mathrm{r_{ct,an}} = \frac{\mathrm{RT}}{2\mathrm{F i_{0,an}^{pre}} \left(\mathrm{x_{H2,bulk}}\right)^{\gamma_{H2}} \left(\mathrm{x_{H2O,bulk}}\right)^{\gamma_{H2O}} \exp\left(-\frac{\mathrm{E_{act,an}}}{\mathrm{RT}}\right)} \tag{26}$$

Reaction orders

By applying logarithms to both sides of Eq. (27), the reaction orders of hydrogen (γ_{H2}) steam (γ_{H2O}) represent the gradient (with opposite sign) of the regression lines in the log-log plots illustrated in Fig. 4 and Fig. 5 respectively.

For a better understanding of what has just been described, the following passage will treat the case of xH_2 variation bearing into mind that the study case for xH_2O is identical. Equation (27) mathematically describes how the charge transfer resistance in the anode varies with the hydrogen partial pressure: it can be appreciated how the plot $\log(x_{H2,bulk})$ vs. $\log(r_{ct,an})$ should theoretically generate a straight line when the cell is operating under constant

temperature and steam partial pressure, hence the first term of the right hand side represents the intercept and γ_{H2} the gradient as above explained.

$$\log(r_{ct,an}) = \log\left(\frac{RT}{2Fi_{0,an}^{pre}\left(x_{H2O,bulk}\right)^{\gamma_{H2O}} exp\left(-\frac{E_{act,an}}{RT}\right)}\right) - \gamma_{H2} \cdot \log\left(x_{H2,bulk}\right) \qquad (27)$$

The experimental results undoubtedly back up this theoretical postulation as seen in Fig. 4 and Fig. 5.

➔ **Figure 4**

The coefficient of determination (R^2) of the regression line generated for the data at 800ºC has a significantly low value (R^2=0.447) hence it has been excluded for the estimation of γ_{H2} whereas the aforementioned coefficient for the rest of the fits have an acceptable value close to R^2=0.900. The estimated reaction order for hydrogen is γ_{H2} =-0.13 and has been calculated by using the average of $\gamma_{H2,750ºC}$ and $\gamma_{H2,700ºC}$, more specifically: -0.158 and -0.095 respectively.

➔ **Figure 5**

As regards the reaction order of steam, the coefficient of determination of the regression line at 750ºC is far too low to be used to estimate γ_{H2O} therefore only the lines fitting the data at 800ºC and 700ºC are employed for this purpose. The appraised reaction order of steam in this work is γ_{H2O}=0.03, denoting that steam plays an inconsequential role in the anodic charge transfer mechanisms as described by the Butler-Volmer equation. *A priori* this makes this cell suitable for operation at high fuel utilizations – where high quantities of steam are produced – hence noticeable electrical efficiencies could be theoretically achieved.

It should be noted that there is a little ambiguity in literature when it comes to associate a value to the reaction orders of hydrogen and steam; a number of authors simply take them *a priori* as one, 0.5 or 0.25 [15,16], however very few authors have really obtained them experimentally. Yamamura *et. al.* [17] for example experimentally calculated a water exponent value (γ_{H2O}) equal to -0.5 whilst Leonide *et. al.* [14] predicted the following exponents: -0.1 for the hydrogen and 0.33 for the water.

Activation energy and pre-exponential factor

The activation energy associated to charge transfer mechanisms in the anode and the pre-exponential factor can be estimated likewise employing Eq. (26) by normalizing both sides as a function of temperature and applying natural logarithms (Eq. (28)). The experimental data obtained from the tests carried out under diverse molar fractions of hydrogen and steam at different temperatures can be plotted in the following way: 1000/T vs. $\ln\left(\frac{r_{ct,an}}{T}\right)$.

$$\ln\left(\frac{r_{ct,an}}{T}\right) = \ln\left(\frac{R}{2Fi_{0,an}^{pre}\left(x_{H2,bulk}\right)^{\gamma_{H2}}\left(x_{H2O,bulk}\right)^{\gamma_{H2O}}}\right) + \frac{E_{act,an}}{RT} \qquad (28)$$

Figure 6 illustrates the previously mentioned plot for the PRN cell when operated under a variation of xH_2, being palpable how a first-order polynomial can adequately fit the data for each individual molar fraction. Attending to what has been just discussed the regression line (best fit) hence can be expressed in the following terms:

$$\ln\left(\frac{r_{ct,an}}{T}\right)\Big|_{fit} = a_0 + a_1\frac{1000}{T} \tag{29}$$

where a_0 and a_1 are constants (intercept and gradient respectively).

It is immediately demonstrated from Eq. (28) and Eq. (29) that the gradient is strictly dependent on the activation energy according to Eq. (30) whilst the intercept is governed by the molar fractions of reacting species and products, their reaction order and the pre-exponential factor as seen in Eq. (31). Therefore the following association can be made:

$$a_1 = \frac{E_{act,an}}{1000 \cdot R} \tag{30}$$

$$a_0 = \ln\left(\frac{R}{2Fi_{0,an}^{pre}\left(x_{H2,bulk}\right)^{\gamma_{H2}}\left(x_{H2O,bulk}\right)^{\gamma_{H2O}}}\right) \tag{31}$$

➔ **Figure 6**

The good agreement in the gradients of the regression lines depicted in Fig. 6 and the superb R^2 indicate that the Arrhenius-type equation is a convincing mathematical manifestation for the modeling of charge transport phenomena in state-of-the-art anodes of SOFCs.

The values obtained from the fitting of experimental results (see Part I of this work) with the theoretical governing equations of the SOFC regarding electrochemistry in the anode are presented in Table 1.

➔ **Table 1**

Charge transfer properties in Ni-YSZ cermets have been regularly studied in the past twenty years and abundant information is available in literature (as an example, Primdahl *et al.* give an extensive overview in [18]). Contemporaneous investigations demonstrate how the anode activation energy lies in the range of 100-150 kJ/mol whilst the exchange transfer current density pre-exponential factor can vary up to several orders of magnitude, from 10^7 to 10^{10} mA/cm^2 [19,20]. The values for $i_{0,an}^{pre}$ and $E_{act,an}$ obtained with the DRT method in this paper fully agree with what has been found in literature, demonstrating once more the soundness of this method to extract qualitative information from EIS measurements.

2.4.2 Cathode exchange current density

The resistance associated to the transfer of charge in the SOFC cathode, expressed by means of Eq. (32), is appraised analogously to that of the anode, specifically, by differentiating the cathode activation overpotential with respect to the current density generated by the electrochemical cell.

$$r_{ct,cat} = \frac{RT}{2Fi_{0,cat}^{pre}\left(x_{O2,bulk}\right)^{\gamma_{O2}} exp\left(-\frac{E_{act,cat}}{RT}\right)} \quad (32)$$

Reaction order

The reaction order of the oxygen (γ_{O2}) can be estimated from the experimental results by applying logarithms to both sides of the preceding equation and expressing the new equation in terms of a first-order polynomial where the variable is the logarithm of the oxygen molar fraction, namely:

$$\log(r_{ct,cat}) = \log\left(\frac{RT}{2Fi_{0,cat}^{pre} exp\left(-\frac{E_{act,cat}}{RT}\right)}\right) - \gamma_{O2} \cdot \log\left(x_{O2,bulk}\right) \quad (33)$$

The slope of the plot $\log\left(x_{O2,bulk}\right)$ vs. $\log(r_{ct,cat})$ effectively designates the value of the reaction order of oxygen attending to Eq. (33). Figure 7 represents the experimental results regarding the activation overpotential in the cathode visualizing the acquired data in terms of the abovementioned plot. It can be appreciated how the regression lines at 700 and 750ºC run astoundingly in parallel with the expected tendency: the first shows higher resistance values than the latter illustrating that operating the cell at higher temperatures enhances the cathode performance. Yet, the data obtained at 800ºC follows a completely non-expected trend providing resistances even higher than the ones obtained at lower temperatures. Withal, the reaction orders of the three different regression lines lie extremely close to each other, ranging from 0.159 to 0.168 and probably what is more important, the coefficient of determination of all the curves is outstanding (R^2>0.990) corroborating the soundness of these values.

➔ **Figure 7**

Activation energy and pre-exponential factor

As has become customary, the electrochemical parameters governing the performance of the cathode are calculated analogously to those of the anode. Equation (32) alongside the plot illustrated in Fig. 8 are employed to obtain the activation energy associated to the activation overpotential in the cathode ($E_{act,cat}$) and the exchange transfer current density pre-exponential factor ($i_{0,cat}^{pre}$).

$$\ln\left(\frac{r_{ct,cat}}{T}\right) = \ln\left(\frac{R}{2Fi_{0,cat}^{pre}\left(x_{o2,bulk}\right)^{\gamma_{H2}}}\right) + \frac{E_{act,cat}}{RT} \quad (34)$$

➔ **Figure 8**

The slopes of the regression lines displayed in Fig. 8 are virtually equal indicating that the activation energy associated to the activation overpotential of the PRN is effectively a constant

value and hence validating to some extent Eq. (34) along with the chosen modeling set of equations. However, it must be noted that only two temperatures have been taken into consideration in the current parameter assessment because the experimental measurements carried out at 800ºC were affected by inconsistent errors.

It can be seen how the term non-dependent from the temperature of Eq. (34) is inversely dependent on the xO_2, thus low values of oxygen molar fraction in the electrochemically active sites should theoretically induce a high charge transfer resistance. This has been confirmed experimentally: the graph portrayed in Fig. 8 depicts this trend.

➔ **Table 2**

2.4.3 Reaction symmetric factor

The theoretical expression for the cell voltage when operating under a particular current density can be expressed in the following terms:

$$V = E_N^{OCV} - \eta_{act,an} - \eta_{act,cat} - \eta_{Ohm} - \eta_{conc,an} - \eta_{conc,cat} \quad (35)$$

where η are the overpotentials.

Nernst voltage

The Nernst voltage when in open circuit voltage and the concentration overpotentials can be unified in one single equation, namely:

$$E_N = E_N^{OCV} - \eta_{conc,an} - \eta_{conc,cat} = E_0 + \frac{RT}{2F} ln\left(\frac{x_{H2,a/e} \cdot x_{O2,c/e}^{1/2}}{x_{H2O,a/e}}\right) \quad (36)$$

where $x_{H2,a/e}$ and $x_{H2O,a/e}$ are the molar fractions of the hydrogen and steam in the anode/electrolyte interface, $x_{O2,c/e}$ the molar fraction of the oxygen in the cathode/electrolyte interface.

Activation overpotentials

When operating at high current densities – hence at high activation overpotentials – the first exponential term of Butler-Volmer expression is significantly bigger than the second, therefore the mentioned equation can be simplified to the following one (taking the name of Tafel equation):

$$\eta_{act} \approx \frac{RT}{\alpha n_e F} ln\left(\frac{i}{i_0}\right) \quad (37)$$

Ohmic overpotentials

The total Ohmic resistance of the cell comprises the resistances of all of the layers composing the SOFC, specifically: anode, electrolyte, diffusion barrier layer and cathode. The cell conductivity can be modeled by means of an Arrhenius equation:

$$\sigma = \frac{\sigma^0}{T} exp\left(\frac{-E_{act,ohm}}{RT}\right) \tag{38}$$

where σ^0 is a constant employed for the best fit of experimental data and $E_{act,ohm}$ is the Ohmic activation energy, obtained from experimental data too.

The Ohmic resistance is obtained from differentiating the Ohmic overpotential with respect to the current density:

$$r_0 = \frac{d\eta_{ohm}}{di} = \frac{d}{di}\left(\frac{i}{\sigma}\right) = \frac{T}{\sigma^0} exp\left(\frac{E_{act,ohm}}{RT}\right) \tag{39}$$

r_0 is the total Ohmic resistance of the cell

➔ **Figure 9**

Experimental results show a very clear trend on how the Ohmic resistance is affected by the operating temperature (Fig. 9); the parameters extracted from the aforementioned graph are tabulated in Table 3.

➔ **Table 3**

Rearranging Eq. (35) and expressing the activation overpotentials in terms of the rest of parameters gives:

$$\frac{RT}{2F\alpha_{an}} ln\left(\frac{i}{i_{0,an}}\right) + \frac{RT}{2F\alpha_{cat}} ln\left(\frac{i}{i_{0,cat}}\right) = E_0 + \frac{RT}{2F} ln\left(\frac{x_{H2,a/e} \cdot x_{O2,c/e}^{1/2}}{x_{H2O,a/e}}\right) - ir_0 - V \tag{40}$$

The forward reaction symmetric factors can be extracted from the experimental data obtained in the polarization curves. In particular, by selecting two high current densities so that the Tafel equation can be employed, the set of two equations with two unknowns (α_{an} and α_{cat}) can be solved.

➔ **Table 4**

The forward reaction symmetric factors for the Ni-YSZ anode and the $Pr_2NiO_{4+\delta}$ are respectively: $\alpha_{an} \approx 0.5$ and $\alpha_{cat} \approx 0.4$ confirming how the fuel electrode performs equally for SOFC and SOEC modes whilst the air electrode is slightly more prone towards electrolysis [21]. Xiao *et al.* experimentally evaluated the effect of temperature on the reaction symmetric factors of state-of-the-art Ni-YSZ electrodes in [22] and observed how α_{an} ranged from 0.46 to 0.54 between 850ºC and 700ºC.

3. Conculsions

The analytical methodology addressed in this paper enables to estimate most of the microstructural and electrochemical features of state-of-the-art solid oxide fuel cells, reducing to a minimum the number of parameters that need to be assumed or obtained from literature to fully characterize an SOFC. Moreover, the aforementioned method permits to appraise factors that would be unbearable to obtain otherwise on a complete cell, such as the reaction orders, activation energies, pre-exponential factors and reaction symmetric factor. Additionally the tortuosity can be comprehensively assessed without the needs of exclusive electronic microscope instrumentation capable of generating 3D reconstructions of micro and nano-scale volumes. Withal, regardless of the potentialities of this analysis method, it needs to be supported with complementary techniques and methods such as the four-point resistivity measurement for the obtainment of the electrical and ionic conductivities of the different materials or FIB-SEM imaging to obtain more accurate values of porosity, particle radii and volume fraction of the electronic and ionic conducting phases.

Acknowledgements

This work was partially supported by the European Commission through the FP7 Infrastructures Programme, Grant Agreement 284522 (H2FC Infrastructures).

Nomenclature

a_0	Intercept of first-order polynomial
a_1	Gradient of first-order polynomial
CFD	Computational Fluido-Dynamic
CHP	Combined Heat and Power
CNLS	Complex Nonlinear Least Squares
CPE	Constant phase element
$D_{k,l}$	Binary diffusion coefficient between species *k* and *l*
$D_{Kn,k}$	Knudsen diffusion coefficient of species *k*
DGM	Dusty Gas Model
DRT	Distributed Relaxation Times
E_{act}	Activation energy
E_N	Nernst potential
E_0	Standard potential
ECM	Equivalent Circuit Model
EIS	Electrochemical Impedance Spectroscopy
F	Faraday's constant
GDC	Gadolinium Doped Ceria
i	Current density
i_0	Local exchange transfer current density
$\vec{J}_k$	Diffusive flux of species *k*
L	Electrode's thickness
MSMM	Modified Stefan Maxwell Model
MW_k	Molecular weight of species *k*
n_e	Number of electrons participating in the electrochemical reaction
OCV	Open circuit voltage
ODE	Ordinary Differential Equation
P	Total pressure

p_k	Partial pressure of species *k*
PDE	Partial Differential Equation
PRN	Praseodymium Nickelate Oxide
R	Ideal gas constant
R_{ct} or r_{ct}	Charge transfer resistance
R_0 or r_0	Ohmic resistance
R_{conc} or r_{conc}	Concentration resistance
SOFC	Solid Oxide Fuel Cell
T	Absolute temperature
TPB	Triple phase boundary
V	Cell voltage
W	Warburg element
x_k	Molar fraction of species *k*
YSZ	Yttria Stabilized Zirconia
z	Position along the electrode

α	Reaction symmetric factor
β	Coefficient accounting for the deviation from equimolar flux.
γ_k	Reaction order of species *k*
ε	Porosity
η	Overpotential
σ	Conductivity
$\breve{\sigma}_k$	Collision diameter of species *k*
τ	Tortuosity

Subscripts

act	Activation
an	Anode
bulk	Gas composition in the electrode/gas channel interface
cat	Cathode
conc	Concentration
el	Electronic
io	Ionic
ohm	Ohmic
pol	Polarization
ref	Reference

Superscripts

eff	Effective
pre	Pre-exponential factor

References

[1] H. Yokokawa, T. Horita, K. Yamaji, H. Kishimoto and M.E. Brito. *Degradation of SOFC Cell/Stack Performance in Relation to Materials Deterioration,* J. of the Korean Ceramic Soc. Vol. 49, No. 1, pp. 11-18 (2012).

[2] P. Holtappels and S. Steinberger-Wilckens. *Realising Reliable, Durable energy Efficient and Cost Effective SOFC Systems (Real-SOFC),* Fuel Cells Vol.9, No. 6, pp. 783-784 (2009).

[3] E. Achenbach. *Three-dimensional and time-dependent simulation of a planar solid oxide fuel cell stack*, J. of Power Sources Vol.57, No. 1-2, pp. 333-348 (1994).

[4] A.V. Virkar, J. Chen, C.W. Tanner and J.W. Kim. *The role of electrode microstructure on activation and concentration polarization in solid oxide fuel cells*, Solid State Ionics Vol. 131, No. 1-2, pp. 189-198 (2000).

[5] H. Yakabe, M. Hishinuma, M. Uratani, Y. Matsuzaki and I. Yasuda. *Evaluation and modeling of performance of anode-supported solid oxide fuel cell*, J. of Power Sources Vol. 86, No. 1-2, pp. 323-431 (2000).

[6] K. Tseronis, I. Bonis, I.K. Kookos and C. Theodoropoulos*. Parametric and transient analysis of non-isothermal, planar solid oxide fuel cells*, Int. J. of Hydrogen Energy Vol.37, pp. 530-547 (2012).

[7] Y. Shi, N. Cai and C. Li. *Numerical modeling of an anode-supported SOFC button cell considering anodic surface diffusion*, J. of Power Sources, Vol. 164 pp. 639-648 (2007).

[8] T. Xiao-Wu, S. Zu-Feng and C. Guan-Chu. *Simulation of the relationship between porosity and tortuosity in porous media with cubic particles*. Chin. Phys. B., 21 (10), p. 100201 (2012).

[9] R. Suwanwarangkul, E. Croiset, M.W. Fowler, P.L. Douglas, E. Entchev and M.A. Douglas. *Performance comparison of Fick's, dusty gas and Stefan-Maxwell models to predict the concentration overpotential of a SOFC anode*, Journal of Power Sources, 122, pp. 9-18 (2003).

[10] T. Graham. *On the motion of gases*. Phil. Mag., 2:175, 269,351, reprinted in "Chemical and Physical Researches", pp. 44-70, Edinburgh Univ. Press, Edinburgh (1876).

[11] Y. Shi, N. Cai and C. Li. *Numerical modeling of an anode-supported SOFC button cell considering anodic surface diffusion*, J. of Power Sources, Vol. 164 pp. 639-648 (2007).

[12] R.E. Williford and L.A. Chick*. Surface diffusion and concentration polarization on oxide-supported metal electrocatalyst particles*, Surface Science, Vol. 547, pp. 421-437 (2003).

[13] P. Chinda, S. Chanchaona, P. Brault and W. Wechsatol. *Mathematical Modeling of a Solid Oxide Fuel Cell with Nearly Spherical-Shaped Electrode Particles*, J. of Sustainable Energy and Environment Vol. 1 pp. 185-196 (2010).

[14] A.Leonide. *SOFC Modelling and Parameter Identification by means of Impedance Spectroscopy*, PhD Thesis, KIT Scientific Publishing.

[15] E. Hernández-Pacheco, M.D. Mann, P.N. Hutton, D. Singh and K.E. Martin. *A cell-level model for a solid oxide fuel cell operated with syngas from a gasification process*. Int. J. of Hydrogen Energy, 30, pp. 1221-1233 (2005).

[16] M.M. Hussain, X. Li and I. Dincer. *Mathematical modeling of planar solid oxide fuel cells*. Journal of Power Sources, 161, pp. 1012-1022 (2006).

[17] T. Yamamura, H. Tagawa, T. Saito, J. Mizusaki, K. Kamitani, K. Hirano, S. Ehara, T. Takagi, Y. Hishinuma, H. Sasaki, T. Sogi, Y. Nakamura and K. Hashimoto. *Reaction Kinetics at the Nickel Pattern*

Electrode on YSZ and its dependence on Temperature. Solid Oxide Fuel Cells IV, M. Dokiya, O. Yamamoto, H. Tagawa and S.C. Singhal. Editors, PV 95-1, pp. 741-749, The Electrochemical Society Proceeding Series, Pennington, NJ (1995).

[18] S. Primdahl. *Nickel/Yttria-stabilised zirconia cermet anodes for solid oxide fuel cells*, PhD Thesis, University of Twente, The Netherlands (1999).

[19] P. Costamagna and K. Honegger. *Modeling of solid oxide heat exchanger integrated stacks and simulation at high fuel utilization*, J. Electrochem. Soc., Vol. 145, No. 11 pp. 3995-4007 (1998).

[20] S. Campanari and P. Iora. *Definiton and sensitivity analysis of a finite volume SOFC model for a tubular cell geometry*, J. of Power Sources, Vol. 132 pp.113-126 (2004).

[21] A.J. Barda and L.R. Faulkner. *Electrochemical Methods – Fundamentals and Applications*, John Wiley & Sons, 2nd Edition, New York (2001).

[22] H. Xiao, T.L. Reitz and M.A. Rottmayer. Polarization measurements of anode-supported solid oxide fuel cells studied by incorporation of a reference electrode, J. of Power Sources, Vol. 183, No.1, pp. 49-54 (2008).

FIGURES

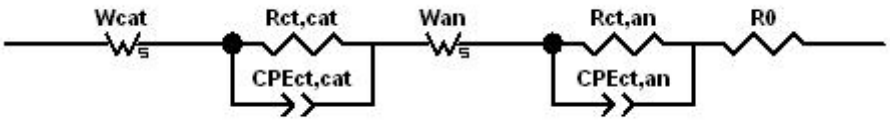

Fig.1. Equivalent Circuit Model (ECM) of the PRN cell

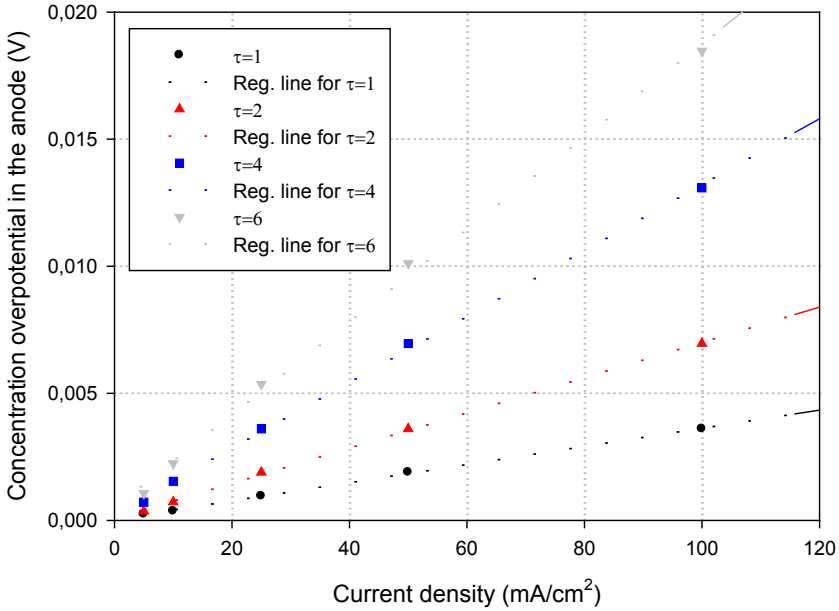

Fig.2. Concentration overpotential in the anode as a function of current density and tortuosity.

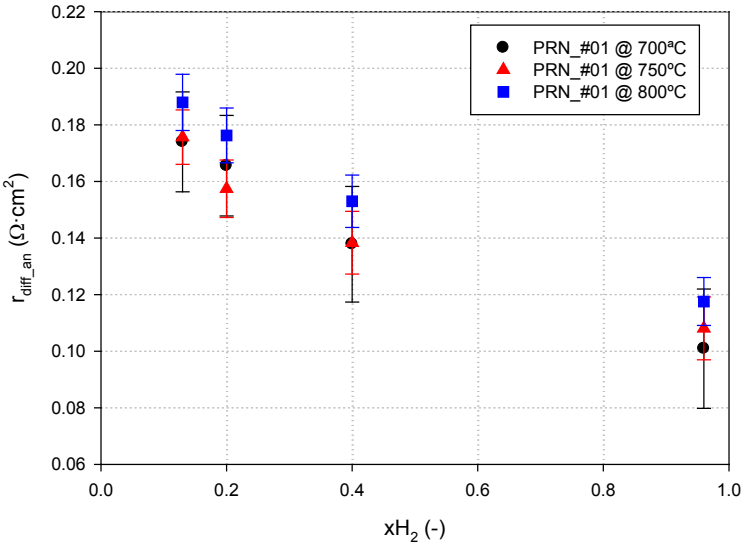

Fig.3. Resistance to the gas diffusion in the anode as a function of hydrogen molar fraction at 800, 750 and 700ºC

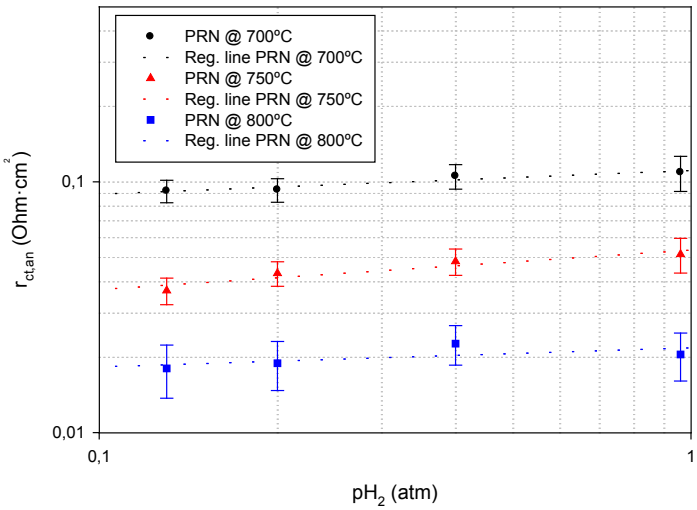

Fig.4. Charge transfer resistance in the anode of the PRN cell as a function of the hydrogen partial pressure at 800, 750 and 700ºC

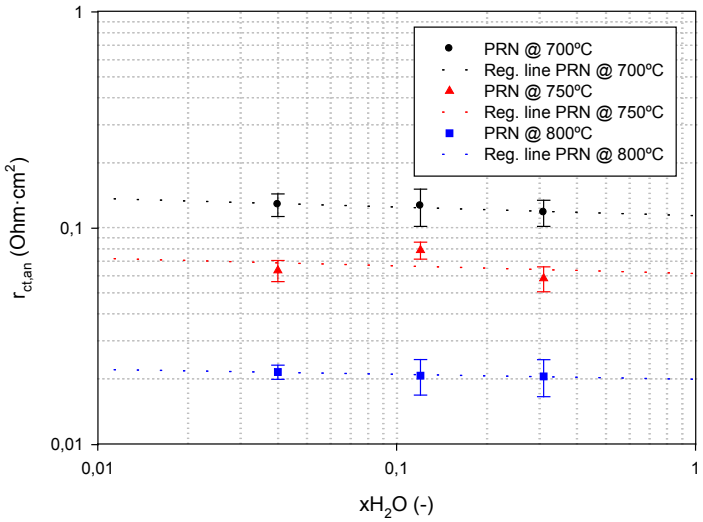

Fig. 5. Charge transfer resistance in the anode of the PRN cell as a function of the water vapour partial pressure at 800, 750 and 700ºC

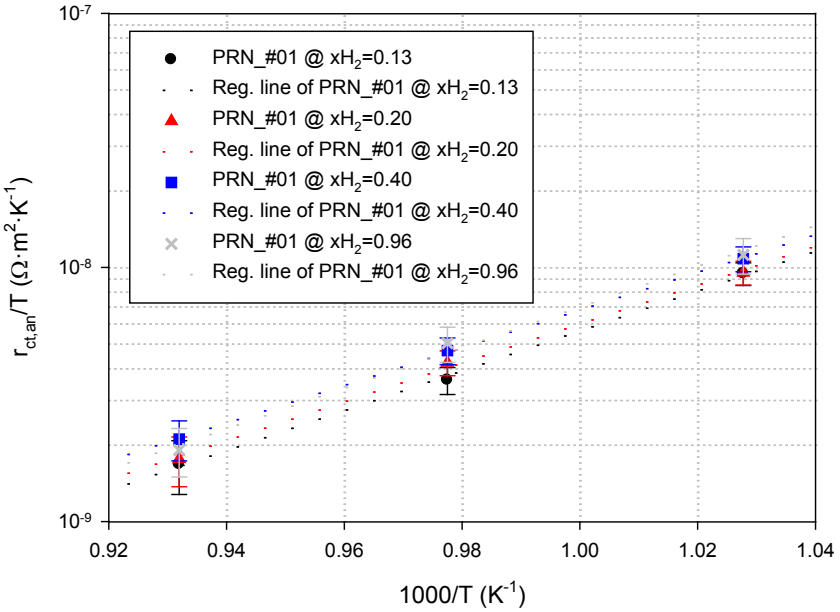

Fig. 6. Charge transfer resistance in the anode of the PRN cell as a function of the temperature for different hydrogen molar fractions.

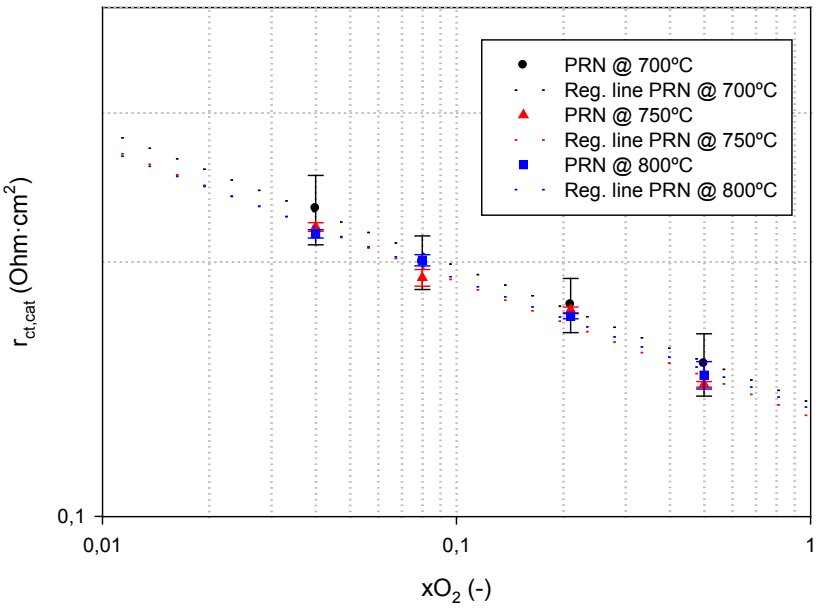

Fig.7. Charge transfer resistance in the cathode of the PRN cell as a function of the oxygen partial pressure at 800, 750 and 700ºC

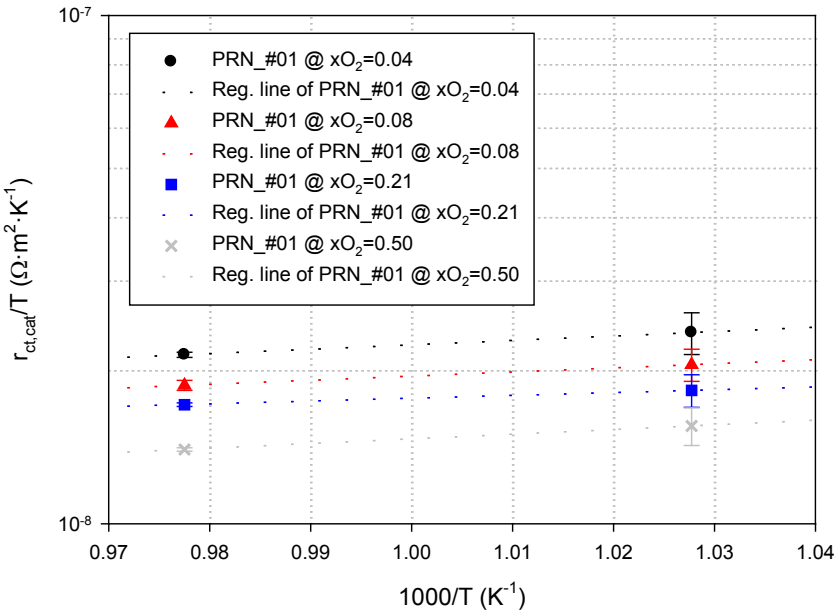

Fig. 8. Charge transfer resistance in the cathode of the PRN cell as a function of the temperature for different oxygen molar fractions.

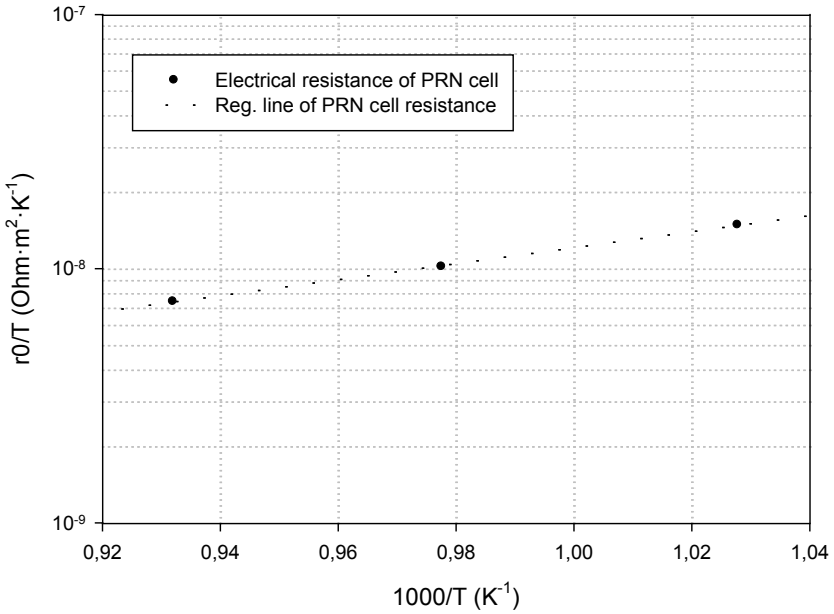

Fig.9. Electrical resistance of the PRN cell as a function of the operating temperature

TABLES

Anode electrochemical parameters	
$i_{0,an}^{pre}$(mA/cm²)	$5.51 \cdot 10^{10}$
γ_{H2}	-0.13
γ_{H2O}	0.03
$E_{act,an}$ (kJ/mol)	147.1

Table 1. Parameters for the anode's Butler-Volmer equation

Cathode electrochemical parameters	
$i_{0,cat}^{pre}$(mA/cm²)	$2.37 \cdot 10^{3}$
γ_{O2}	0.16
$E_{act,cat}$ (kJ/mol)	16.6

Table 2. Parameters for the cathode's Butler-Volmer equation

Cell's Ohmic resistance parameters	
σ^0(S·K/m²)	$1.1575 \cdot 10^{10}$
$E_{act,Ohm}$ (kJ/mol)	43.32

Table 3. Parameters in the Arrhenius equation describing the cell's Ohmic resistance

Current density (mA/cm²)	$x_{H2,a/e}$	$x_{H2O,a/e}$	$x_{O2,c/e}$	V **(V)**
1500	0.8078	0.1922	0.1907	0.721
1600	0.7994	0.2006	0.1894	0.707

Table 4. Measured cell voltage and molar fractions of the species in the electrode/electrolyte interface